Nonlinear Buckling and Postbuckling Analysis of Tow-Steered Composite Cylinders with Cutouts

Rainer M.J. Groh*
Bristol Composites Institute, University of Bristol, Bristol, BS8 1TR, UK

K. Chauncey Wu†
NASA Langley Research Center, Hampton, VA 23681, USA

The buckling and postbuckling behavior of two composite tow-steered shells with cutouts of different sizes is assessed using nonlinear finite element (FE) analysis and compared to experimental measurements. The cylindrical shells are manufactured using an automated fiber placement system, where the shells' fiber orientation angles vary continuously around the shell circumference from ± 10 degrees on the crown and keel to ± 45 degrees on the sides. One shell features thickness variations due to tow overlaps that result from application of all 24 tows during each pass of the fiber placement system. The second shell uses the system's tow drop/add capability to achieve a more uniform wall thickness without overlaps. Unreinforced cutouts of two different sizes—the first smaller cutout representing a passenger door on a commercial aircraft and the second larger cutout a cargo door—were machined into each of the two cylinders resulting in a total of four test cases. These cylinders were tested in axial compression and buckled elastically in previous work and are now analyzed using nonlinear FE models to compare bifurcation buckling loads as well as the load-displacement response in the prebuckling and postbuckling regimes. For all four shells analyzed, the prebuckling stiffness, buckling load, and deformation mode sequence throughout the loading-unloading cycle is accurately reproduced by the models. In particular, the shells first buckle locally around the cutouts in a stable (super-critical) manner with only a slight decrease in axial stiffness, which occurs due to the favorable load redistribution facilitated by tow steering. The shells then buckle globally in an unstable (sub-critical) manner with diamond-shaped buckles forming to the left and right (circumferential direction) of the cutouts. The buckling load of all shells with cutouts is at least 82% of the buckling load of the pristine shells without cutouts. Overall, the ability to sustain local buckling phenomena, and the relatively small reductions in global buckling load compared to pristine shells without cutouts, demonstrates the great potential of using tow

*Lecturer in Digital Engineering of Structures, Department of Aerospace Engineering. Corresponding author: rainer.groh@bristol.ac.uk.
†Acquisition Manager, Science Office for Mission Assessments. AIAA Associate Fellow.
Parts of this work were presented at the AIAA SciTech 2022 Forum, San Diego, CA, USA, 3–7 January, 2022. Paper nr. 2148 [1].

steering to mitigate the adverse effects of cutouts in axially-compressed shell structures.

I. Introduction

Cutouts are typical features in thin-walled aerospace structures such as aircraft fuselages and launch vehicles, and range from windows and passenger/cargo doors to access holes for maintenance/inspection. The discontinuity introduced by the cutout generally leads to stress concentrations, or at the very least, load redistributions that adversely affect the overall structural performance. Traditionally, these adverse effects are overcome by surrounding the cutout with additional reinforcing material [2]. A more efficient solution from an overall mass perspective would be to redirect some of the load away from the cutout using, for example, elastic tailoring through stiffness variations. Recently, such approaches have become more viable by advancements in automated manufacturing processes. For example, localized 3D-printed [3] or stitched carbon fiber reinforcements [4] can be used to reduce stress concentrations around open holes. Alternatively, automated fiber placement machines can steer tows of pre-impregnated fiber-reinforced plastic in curvilinear trajectories and thereby use the orthotropic nature of composites to redirect loads around, or even away, from cutouts [5, 6]. In this manner, additional reinforcements and their associated mass penalty can be minimized.

In traditional composite material design, a laminate is created by stacking an integer number of unidirectional plies, where the fiber angle of each ply can be optimized to best serve the structural requirements of the laminate. To further increase the possible design space for elastic tailoring, automated tow deposition systems can be used to continuously vary the fiber direction over the planform of each ply [7]. These computer-controlled machines place a large number of continuous and unidirectional composite tows onto a tool surface, whilst also precisely and accurately following predefined curvilinear spatial paths. Currently, the two most commonly used methods to create large-scale tow-steered laminates are automated fiber placement (AFP) [7], which uses in-plane bending of tows to achieve steering, and continuous tow shearing (CTS) [8], which uses incrementally applied in-plane shearing to control the tangent direction of a tow path. Other methods that have been developed for manufacturing variable-stiffness structures based on curved fiber trajectories include tailored fiber placement [4] and variable-angle filament winding [9].

Even though tow-steered composites have attracted increasing research attention over the last two decades [10], including applications to panels with open holes [11–13], buckling of flat and curved compression panels [14–27], pressure vessels [28, 29], cylinders under bending [30], compression [31–37] and vibration [33, 38], and aircraft wings [39–46], experimental data that can be used to validate different design, modeling and analysis approaches are relatively rare. Therefore, the steps and techniques required for commercial certification of tow-steered composite parts are not as well defined or understood as for established straight-fiber composites. Recent steps in this direction have been taken, for example, by Çelebi *et al.* [47] and Labans *et al.* [48], who, respectively, conducted buckling and progressive failure analyses of a tow-steered cylindrical shell with circular cutouts under global bending and then validated the models with experiments. To further expand the current state of knowledge, the aim of the current work is to showcase

the potential of ameliorating some of the adverse structural effects associated with cutouts in thin-walled structures, and to help expand the database of practical experience in modeling the nonlinear buckling response of tow-steered cylinders.

In previous work, two prototype tow-steered composite cylinders (without cutouts) were designed [49], manufactured [50], and experimentally evaluated under displacement-controlled end-shortening and buckled elastically [31]. The cylindrical shells were manufactured using an AFP system, where the shells' fiber orientation angles were changed continuously around the shell circumference from ±10 degrees on the crown and keel to ±45 degrees on the sides. One shell (Shell A) features thickness variations due to tow overlaps that resulted from application of all 24 tows during each pass of the fiber placement system. The second shell used the system's tow drop/add capability to achieve a more uniform wall thickness without overlaps (Shell B).

Detailed nonlinear FE analyses of these baseline shells were then performed to corroborate the experimental results and provide physical insight into the mechanism driving the buckling behavior of the shells. In particular, White *et al.* [32] investigated the symmetry-breaking effect of the circumferential stiffness variation facilitated by the tow-steered designs. In contrast to a constant-stiffness cylinder (*e.g.*, an isotropic or straight-fiber composite design), in which the strain energy associated with a single buckle in the cylinder wall is invariant to circumferential translations, the nonuniform stiffness distribution in tow-steered cylinders favors the formation and "trapping" of buckles in the most highly-loaded regions around the circumference. This characteristic of tow-steered cylinders may explain their relatively low imperfection sensitivity when compared to isotropic or quasi-isotropic cylinders [35, 51], as the adverse effect of geometric imperfections is limited to a small portion of the total cylinder surface.

The observed prebuckling, global buckling and postbuckling behaviors for both baseline shells (Shells A and B) described in previous work were found to be elastic with no visible indication of material damage. To use these shells for additional structural tests, the same composite shells were then modified by introducing unreinforced, scaled passenger-door-size cutouts into both shells (so-called "small" cutouts) [52], followed by further axial compression tests to buckle the shells. To prevent damage, the applied end-shortening was reversed immediately after global buckling occurred. The size of the cutouts was subsequently enlarged into unreinforced, scaled cargo-door-size cutouts (so-called "large" cutouts) for further compression buckling tests [53].

Hence, a total of four test cases with cutouts were performed—two shells (Shell A and Shell B) with two different cutouts (small and large). To date, the compression tests of these tow-steered composite shells with small and large cutouts have been compared with linear FE models to assess axial stiffness, strain fields and linear bifurcation buckling load predictions [52, 53]. In the present work, the analysis of these four test cases is extended into the geometrically nonlinear regime to model the complete loading-unloading cycle, *i.e.*, prebuckling stiffness, buckling load, restabilized postbuckling load, and sequence of deformation modes from prebuckling into the postbuckling regime.

It is worth noting that (i) the radius-to-thickness ratio of actual aircraft fuselages is typically greater than the

specimens analyzed here; (ii) aircraft fuselages are stiffened rather than monocoque shells; and (iii) loading is multi- rather than uni-axial. However, in order to test the effect of tow-steering in isolation—without the additional effect of stiffeners—under the challenging load case of axial compression that is strongly influenced by imperfections, the current work is still highly relevant for the design of future aircraft and launch vehicle structures.

The rest of the paper is organized as follows. Section II describes the geometry of the shell, the manufactured cutouts, and fiber trajectories. Section III then summarizes the experimental setup of the compression buckling tests, while Section IV describes the nonlinear FE model in Abaqus. Experimental and analytical results are then compared in Section V, and conclusions are drawn in Section VI.

II. Tow-Steered Shell Description

A. Pristine Baseline Shells (Shell A and Shell B)

Two cylindrical laminated composite shells were manufactured using an AFP system, as described in Ref. [50]. Half of the plies in the composite stacking sequence are classic straight-fiber plies, while the other half of the laminate features fiber orientation angles that vary continuously around the cylinder circumference. The nominal laminate thickness is 1.016 mm, with a nominal inner diameter of 413.16 mm and 889 mm overall length. The shells are manufactured using 3.175 mm-wide IM7/8552 graphite/epoxy slit tape material oriented in a nominal eight-ply $[\pm 45/\pm\Theta(y)]_s$ layup, where Θ is the steered fiber orientation angle that varies along the circumferential coordinate y. The function describing the fiber orientation $\Theta(y)$ is a piece-wise continuous function defined at the following circumferential locations,

$$\Theta\left(y = 0, \frac{\pi R}{2}, \pi R, \frac{3\pi R}{2}, 2\pi R\right) = (10^\circ, 45^\circ, 10^\circ, 45^\circ, 10^\circ), \tag{1}$$

where the 0 degree direction coincides with the axis of the cylinder. Between the circumferential positions defined in Eq. (1), the fiber angles vary continuously between the quoted fiber angles. Hence, the fiber orientation angle Θ is steered to vary continuously from 10 degrees on the shell crown and keel to 45 degrees on the shell sides along a constant-radius circular arc, as illustrated in Fig. 1. The overall stacking sequence results in a laminate with high axial membrane and bending stiffness at the crown and keel (local layup $[\pm 45, \pm 10]_s$), varying to a high in-plane shear and twisting stiffness at the sides (local layup $[(\pm 45)_2]_s$). As described in Ref. [49], one possible application for this type of structure could be an advanced commercial aircraft fuselage, with the fuselage assumed to behave like a beam in bending under the applied flight loads. In this application, the fuselage crown and keel experience longitudinal compression and tension loads, and the shell sides are subjected to shear as the loads transfer between the crown and keel. The experimentally measured reference material properties used for the shell finite element analyses in Section V are taken from Ref. [32] and reproduced in Table 1.

During fabrication, a maximum of 24 tows are placed by the fiber placement system at each location on the shell

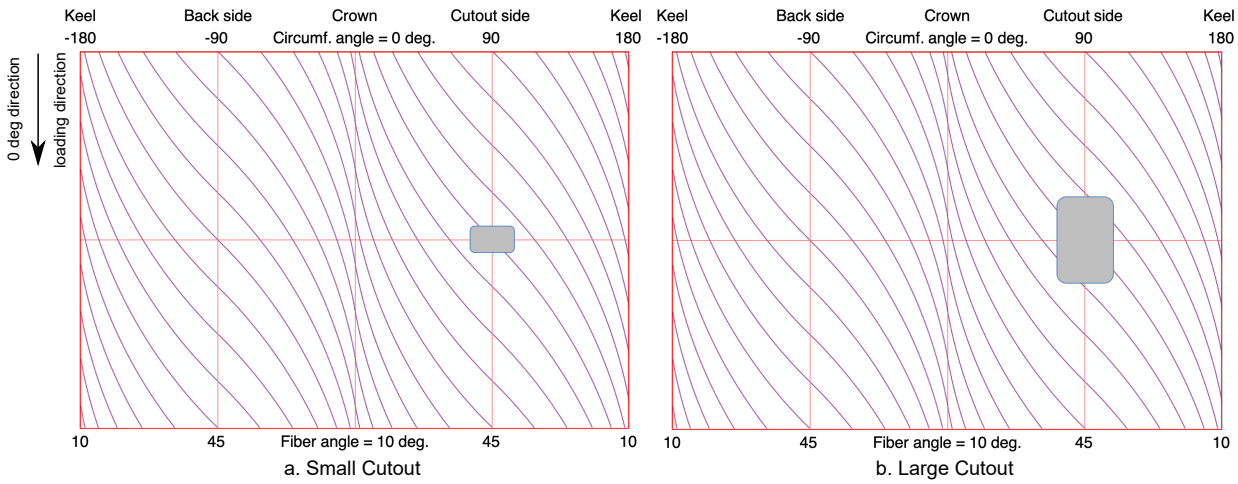

Fig. 1 Planform of the cylinder with (a) small cutout and (b) large cutout. The fiber orientation angle Θ, which varies continuously from 10 degrees on the shell crown and keel to 45 degrees on the shell sides along a constant-radius circular arc, is shown for both cylinders. The full stacking sequence contains both ±Θ plies.

Table 1 Material properties of IM7/8552 graphite/epoxy slit tape material (taken from [32]).

E_{11} (GPa)	E_{22} (GPa)	G_{12} (GPa)	G_{13} (GPa)	G_{23} (GPa)	ν_{12}	t_{ply} (mm)
134.3	9.38	5.21	5.21	4.00	0.347	0.127

planform. When all 24 tows are placed during each pass of the fiber placement system (also called a course), a regular pattern of thicker regions (up to 16 plies, or 2.032 mm thickness, with effective stacking sequence $[\pm 45, 10_3, -10_3]_s$) is generated between adjacent courses on the shell crown and keel regions, as shown in Fig. 2. However, there are no tow overlaps along the shell sides where individual tows tessellate. These overlaps occur as a natural side effect of steering tows by in-plane bending. Due to the finite width of a tow course, inner and outer edges of a tow lie on different radii of curvature. If a new tow course is deposited and placed adjacent to a previous course by shifting it perpendicular to the steering direction, then the inner fibers of the new course and the outer fibers of the old course will have to overlap somewhere due to their different radii of curvature. Put differently, the spacing between fiber paths is not constant, such that two constant-width tow courses that are adjacent at the widest spacing naturally overlap as the fiber paths converge. The resulting laminate thickness build-ups led to designation of this test specimen as the shell with overlaps (Shell A). Alternatively, individual tows in a course can be cut ("dropped") or added at various points during steering. While this approach eliminates overlaps and leads to a more uniform laminate thickness, it also creates small resin-rich pockets that may serve as local crack-initiation sites. Usage of this tow-dropping capability led to designation of the second test specimen as the shell without overlaps (Shell B).

Structural testing of Shell A and Shell B in axial compression is described in Ref. [31]. Both shells were encased in epoxy at their extremities over a length of 25.4 mm in-between two aluminum rings, in order to apply a fully-clamped boundary condition. The ends of the cylinder-potting assembly were then machined to be flat and parallel to each other.

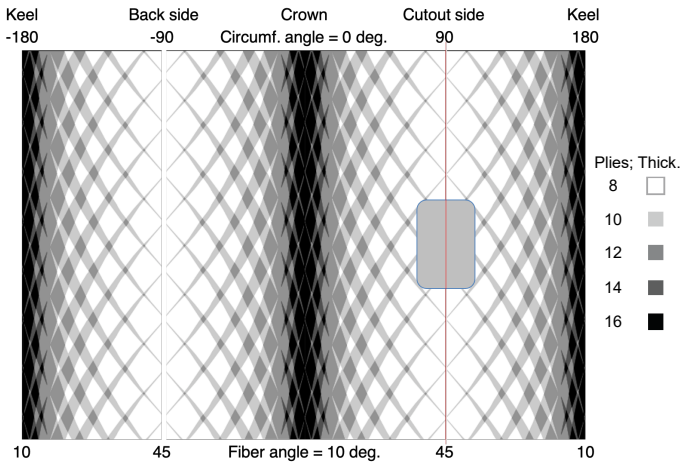

Fig. 2 Planform view of Shell A (with large cutout) showing the varying thickness profile that is incurred due to overlaps of individual tow courses during tow steering using a constant radius of curvature and shifting of individual tow passes. Darker shades of color denote a thicker wall thickness towards the crown and keel.

The cylinders were placed upright into an axial compression machine between two rigid platens. One platen was fixed in all degrees of freedom, and the other platen translated only along the shell axis to apply displacement-controlled end-shortening beyond the onset of buckling and into the postbuckling regime. Once the buckling tests on Shell A and Shell B were completed and the shells were unloaded, flash thermography was performed to identify any potential internal damage caused by these compression tests. No obvious damage to either shell was noted during this assessment.

B. Shell A and Shell B with Small Cutouts

After structurally testing the two baseline shells and making sure that no internal damage was incurred, a single cutout was machined into the center of one side of each shell (*i.e.*, the cutout side, see Fig. 1a) where the layup is approximately $[(\pm 45)_2]_s$. These cutouts are sized and oriented to represent a passenger access door on a commercial aircraft, and measure 76.2 mm along the shell longitudinal dimension by 123.8 mm in the circumferential dimension, with 12.7 mm corner radii. These shells are henceforth referred to as Shell A and Shell B with "small" cutouts (Shell A-Small and Shell B-Small). The shell "back side" is defined to be diametrically opposite to the cutout side (see notation in Figs 1 and 2). The region around the cutouts was repainted with a black base coat and speckled for measurements gathered with three-dimensional digital image correlation (DIC) systems during compression testing. Additional strain gages were also installed around the cutout to measure the local strain responses. Both Shell A-Small and Shell B-Small were then retested using the same test setup and procedure as for the pristine shells described above. This test campaign is described in detail in Ref. [52]. Of particular note is that both Shell A-Small and Shell B-Small were immediately unloaded once global buckling occurred in order to minimize the likelihood of structural damage around the cutouts. Flash thermography was again performed to identify any potential internal damage caused during these tests. No obvious damage to either shell was noted, either visually or from the thermographic inspection.

C. Shell A and Shell B with Large Cutouts

Following the structural testing and non-destructive examination of Shell A and Shell B with small cutouts, a single large cutout, completely surrounding each previous smaller cutout, was machined into the center of one side of each shell, as shown in Fig. 1b. These shells are henceforth referred to as Shell A and Shell B with "large" cutouts (Shell A-Large and Shell B-Large). The cutouts were scaled and oriented to represent a cargo door on a commercial aircraft, and measured 203.2 mm along the shell longitudinal dimension by 133.4 mm in the circumferential dimension, with 19.1 mm corner radii. Both Shell A-Large and Shell B-Large were then retested using the same test setup and procedure as for the pristine shells, and the test campaign is described in detail in Ref. [53]. As was the case for the shells with small cutouts, Shell A-Large and Shell B-Large were axially compressed until global buckling occurred and then immediately unloaded.

III. Experimental Testing Campaign

Initial compression tests of the pristine tow-steered shells without cutouts were performed to evaluate their structural performance, and presented in Ref. [31]. In these baseline tests, Shell A, the shell with overlaps, exhibited a linear prebuckling axial stiffness of 93.0 kN/mm (least-squares best fit to prebuckling data after machine settling to avoid initial nonlinearity), and buckled at 172.6 kN. Shell B, the shell without overlaps, had a prebuckling stiffness of 57.6 kN/mm, and buckled at 76.5 kN. Both shells responded elastically throughout the applied loading, with no indications of material damage visible after the tests concluded. The shells were loaded into deep postbuckling to approximately two times the end-shortening observed at global buckling, but were not loaded to material failure.

The same test setup and hardware described in Ref. [31] was then deployed for the tests of the shells with cutouts, as shown in Fig. 3. Their resulting axial stiffness, buckling and postbuckling behaviors were measured, characterized, and compared with the corresponding baseline data from Ref. [31]. The sets of results with and without cutouts are directly comparable because the same test articles and methodologies were used, with the only difference being the inclusion of the cutouts in the latter test articles.

For the compression tests on the shells with small cutouts, Shell A-Small exhibited a linear prebuckling axial stiffness of 87.1 kN/mm, and buckled at 141.5 kN. Shell B-Small had a prebuckling stiffness of 52.5 kN/mm, with global buckling at 68.9 kN. After these shells buckled and achieved a stable postbuckled state, they were unloaded back to zero load. Both shells again responded elastically, and appeared undamaged after the tests were concluded. The same test setup and hardware was then used again on the shells with large cutouts. In these tests Shell A-Large exhibited a linear prebuckling axial stiffness of 85.6 kN/mm, and buckled at 146.8 kN. Shell B-Large had a prebuckling stiffness of 51.8 kN/mm, with global buckling at 64.9 kN. The experimental results of these six test cases are summarized and compared in Table 2.

Interestingly, the reduction in buckling load due to the introduction of cutouts is between 10–18% and the prebuckling

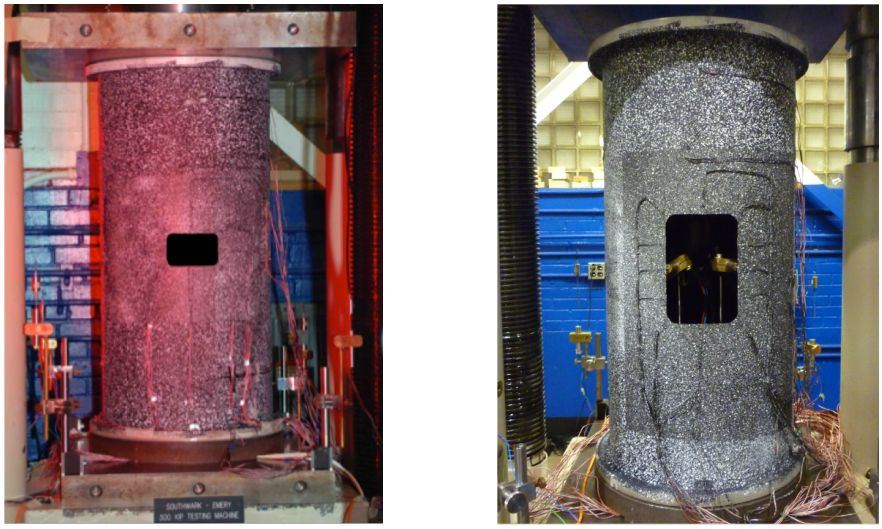

a. Small Cutout b. Large Cutout

Fig. 3 Experimental test setup of a shell with (a) small cutout, and (b) large cutout.

Table 2 Experimental measurements of global buckling load and prebuckling stiffness for Shell A and Shell B with cutouts (small/large) and without cutouts (pristine shell). Percentage reduction in values due to cutouts compared to pristine shell are shown in parentheses. The table shows both absolute (kN & kN/mm) and mass-normalized (kN/kg & kN/mm/kg) values based on the shown shell masses (kg).

Shell Performance	Shell A			Shell B		
Metric	Pristine	Small	Large	Pristine	Small	Large
Prebuckling Stiffness (kN/mm)	93.0	87.1 (-6.3%)	85.6 (-8.0%)	57.6	52.5 (-8.9%)	51.8 (-10%)
Global Buckling Load (kN)	172.6	141.5 (-18%)	146.8 (-15%)	76.5	68.9 (-10%)	64.9 (-15%)
Prebuckling Stiffness (kN/mm/kg)	39.2	36.9 (-5.8%)	36.8 (-6.2%)	30.7	28.2 (-8.2%)	28.3 (-7.8%)
Global Buckling Load (kN/kg)	72.8	60.0 (-18%)	63.1 (-13%)	40.8	37.0 (-9.3%)	35.5 (-13%)
Shell Mass (kg)	2.37	2.36	2.33	1.87	1.86	1.83

stiffness is reduced by 6.3–10%. A first-order approximation based on the reduction in circumferential perimeter due to the cutouts suggests a knockdown in axial stiffness of $\approx 10\%$. All four tow-steered cylinders have a slightly smaller reduction in axial stiffness compared to this first-order approximation because the stiffness variation due to tow steering redistributes the prebuckling stresses away from the geometrically more compliant region (the cutout), such that the structural behavior is dominated by the stiffer regions without cutout. This effect is especially evident in the fact that the prebuckling stiffness and global buckling loads of the shells with small and large cutouts are comparable. Hence, increasing the size of the cutout did not significantly impact the structural response for either Shell A or Shell B. In addition, Table 2 shows that the mass-normalized prebuckling stiffnesses and mass-normalized buckling loads of Shell A and Shell B are less affected by the presence of the cutouts (compare the percentage reductions in parentheses in Table 2) than when these measurements are compared on an absolute basis (without normalizing by mass). Tow steering has therefore counteracted some of the inevitable loss in stiffness that occurred when a portion of Shell A and Shell B was removed by introducing the cutouts.

As expected, the experimental buckling load of Shell B-Small is greater than the buckling load of Shell B-Large. Interestingly, the reverse is true for Shell A, with the large-cutout shell outperforming the small-cutout shell in buckling load. As is shown in the following linearized buckling and geometrically nonlinear analyses, this result is not predicted by the computational models based on a perfect shell geometry. As such, we hypothesize that the machining process for the small cutout created more local imperfections, *e.g.* above and below (axial direction) the cutout, which were then removed when the cutout was enlarged. In addition, loading imperfections also play an important role in knocking down the buckling load, and it is possible that unwanted end-rotations during the tests for Shell A-Small were greater than for Shell A-Large.

IV. Finite Element (FE) Model

The commercial FE software package Abaqus 2018 [54] was used to create converged models of Shell A and Shell B with small and large cutouts, and used to solve for the buckling and postbuckling behavior of the shells. The shell geometries outlined in Section II were meshed using 32,778 S4R and 66 S3R shell elements (198,630 degrees of freedom in total) for the cases with small cutouts, and 28,918 S4R and 40 S3R shell elements (175,770 degrees of freedom in total) for the cases with large cutouts. All nodes lie on a radius of 207.4 mm, which corresponds to the shells' average measured inner line radius (206.9 mm) plus one-half of the nominal eight-ply laminate thickness (0.508 mm). That is, all nodes lie on the nominal cylinder mid-plane reference surface, not accounting for geometric imperfections. The mid-plane of laminates thicker than eight plies are offset towards the shell outer surface, such that the inner surface of the shell is smooth. For all models, a ply thickness of 0.127 mm was used, which results in a minimum and maximum wall thickness of 1.016 mm and 2.032 mm on the sides and crown/keel of Shell A, and a uniform wall thickness of 1.016 mm for Shell B. No geometric imperfections or loading eccentricities were included in the FE models.

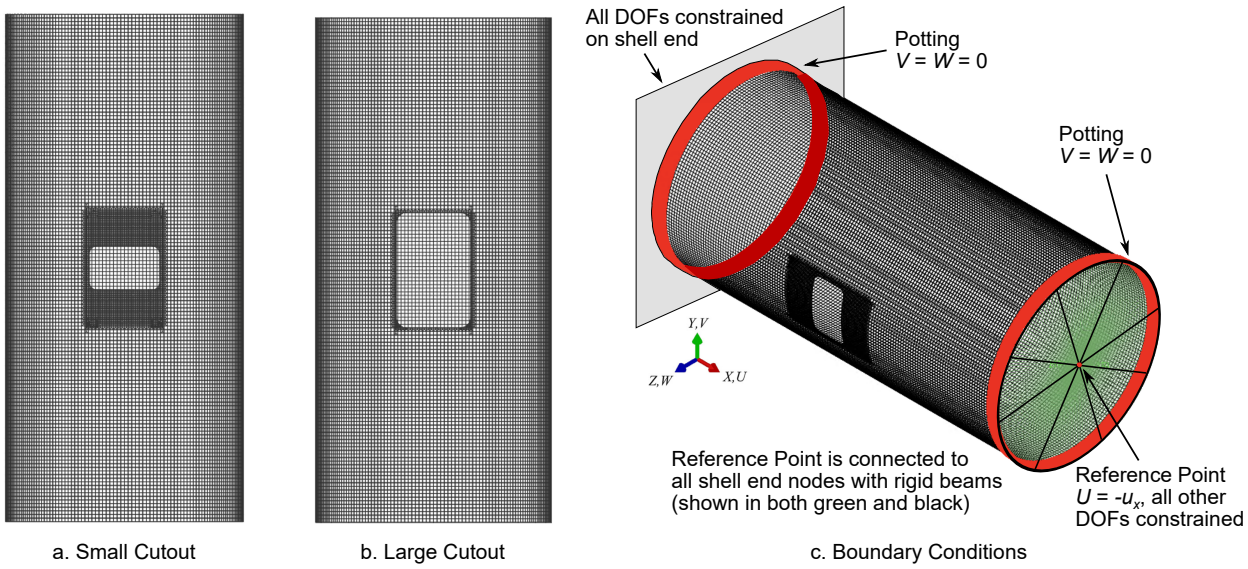

Fig. 4 Meshed cylinders with (a) small cutout and (b) large cutout, showing mesh refinement around the cutouts. (c) Boundary conditions applied in all models, *i.e.*, Shell A-Small, Shell A-Large, Shell B-Small, Shell B-Large.

As shown in Fig. 4a,b, both FE meshes were refined around the cutouts to account for the steeper stress gradients that are expected in these areas. The global mesh density of approximately 6.35 mm × 6.35 mm element area—based on a previously converged mesh of the cylinder without cutouts [32]—was 2×, 3×, and 4× refined around the cutouts. As the relative difference in axial stiffness and global buckling load between 3× and 4× refinement was less than 0.5%, the global mesh of 6.35 mm × 6.35 mm element area with 3× refinement around the cutouts was chosen. The data for the spatial variation of ply thicknesses, total laminate thickness, and ply fiber-angle orientation were obtained from previous characterizations of the shells [31, 49, 50]. As the fiber-angle orientation, and in the case of Shell A also the ply thickness, varies spatially across the shell planform, a unique stacking sequence was created for every element in the mesh. As a constant fiber angle and stacking sequence is used in the interior of every finite element, the FE mesh features a piece-wise constant distribution of stiffness rather than a continuous one. This piece-wise constant, element-by-element definition also means that a sufficiently fine mesh density is required to accurately capture the spatially varying fiber and laminate thickness distributions.

The loading-unloading cycle was modeled using the *Implicit, Dynamic time-integration algorithm implemented in Abaqus 2018 with geometric nonlinearity effects included (no material nonlinearity). To replicate the slow loading rate applied in the experiments, the Quasi-static option is used, in which considerable energy dissipation is applied to provide improved convergence behavior for determining an essentially static loading process. This approach also circumvents the necessity of approximating structural damping rates in the Hilber-Hughes-Taylor (HHT) algorithm [55]. For all models, the maximum amount of end-shortening observed in the experiments was applied via a linearly increasing ramp over a time period of 600 s, after which the end-shortening was reversed in a linearly decreasing ramp of another

600 s.

The boundary conditions applied in the model replicate the experimental conditions as closely as possible. In the experimental tests, the two ends of the cylinder were compressed between two rigid platens, with one end stationary and the other translated axially. In the model this condition was reproduced by completely restraining (clamping) the circumferential nodes at one end of the cylinder. At the other end, a central reference point was connected to the circumferential boundary nodes using a rigid-beam multi-point constraint. The reference point was restrained completely with only axial displacement along the length of the cylinder allowed. This produces the well-known "wheel" effect, with the reference point acting as the "hub" and the rigid beams as the "spokes". To represent the encasement provided by the epoxy potting, all nodes falling with 25.4 mm of the two cylinder ends were also prevented from displacing radially and tangentially. The applied boundary conditions are shown in Fig. 4c.

A further effect of the epoxy potting is that it leads to a local increase in the axial stiffness at the cylinder ends. Generally speaking, this is not expected to have a big influence on the computed buckling loads, but can have an effect on the computed prebuckling stiffness, restabilized postbuckling load, and postbuckling stiffness [32, 56]. After preliminary modeling tests, the effect of locally increasing the axial stiffness in the potting region was not found to have a significant effect on the results, and for simplicity, it was therefore not included in the models.

V. Results

A. Linearized Buckling Analysis

Previous FE analyses in Refs [52] and [53] studied the prebuckling stiffness, prebuckling strain field and linearized buckling response of Shell A and B with small and large cutouts, respectively. Before conducting the nonlinear dynamic analyses in Abaqus 2018, a linearized *Buckle step was performed to corroborate the results found in Refs [52] and [53]. Table 3 shows the linearized buckling loads predicted by the present model in Abaqus 2018, which confirm the previous FE results in Refs [52] and [53]. In particular, for all cases the first linearized buckling load (lowest eigenvalue) corresponds to a single quarter-wave to the left and right (circumferential direction) of each cutout (see Fig. 5a,c,e,g). Hence, the unsupported free edges of each cutout are predicted to buckle first. For all shell-cutout combinations, this local buckling mode occurs for a level of compression well below the global buckling load measured in the tests (compare FE-results Table 3 with test-results Table 2).

For all shells, the second, third, and even higher critical eigenvalues of the linearized buckling analysis correspond to higher-order local buckling modes around each cutout, as discussed in Refs [52] and [53]. The very first global buckling mode that appears in the eigenvalue problem and envelops a large proportion of each shell is shown in Fig. 5b,d,f,h, with the corresponding buckling loads listed in Table 3. These global buckling modes occur in the axially stiffest circumferential regions of the shell domain (crown/keel) where the local layup is $[\pm 45, \pm 10]_s$. The circumferential

Table 3 Linear buckling load predictions from ABAQUS 2018. The first buckling mode is always local around the cutout, and only higher-order eigenvalues correspond to global buckling modes. The global buckling load prediction is compared to the experimental buckling load from Table 2 and is shown in parentheses.

Buckling Load	Shell A		Shell B	
	Small	Large	Small	Large
Local Buckling (kN)	82.7	62.3	44.9	34.9
Global Buckling (kN)	167.3 (18%)	165.5 (13%)	69.8 (1.3%)	68.9 (6.2%)

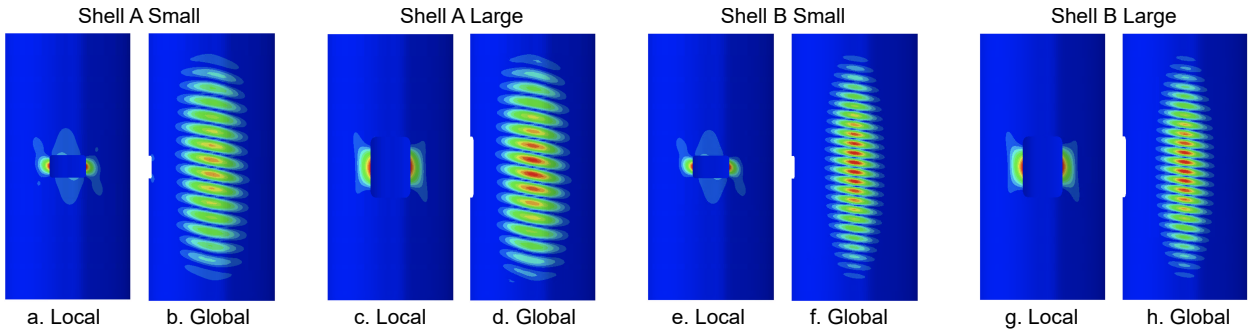

Fig. 5 (a)-(h) Local and global buckling modes for Shell A and Shell B with small and large cutouts as computed by ABAQUS 2018 in a linearized buckling analysis.

stiffness variation induces a non-uniform prebuckling stress field, with the axially stiffest regions attracting the greatest axial load under uniform end-shortening, such that buckling is "trapped" [32] in this highly-loaded region. To provide physical insight into the global buckling modes observed in Fig. 5b,d,f,h we can make an analogy to the buckling response of a beam on an elastic foundation. Due to the narrow and elongated nature of the global buckling modes, axial strips of the cylinder surrounding the crown/keel are assumed to represent a straight beam and the circumferential hoop stiffness of the cylinder is assumed to act as an elastic foundation. This beam-on-an-elastic-foundation system is known to form short wavelength buckles when axially compressed, as a result of an energy trade-off between minimizing the strain energy in the beam (curvature driven, long wavelength) and minimizing the strain energy in the foundation (spring-elongation driven, short wavelength).

The global buckling load predictions from the linearized eigenvalue analysis in Table 3 are always significantly greater than the first local buckling mode around the cutouts. This shows the great promise of tow steering in redistributing internal load paths—in this case, away from the cutouts to the stiffer crown/keel regions—such that local buckling events around the cutouts have a smaller effect on the residual load-carrying capacity. However, the global buckling loads predicted by the linearized buckling analysis always over-predict the buckling loads measured in the tests (see values in parentheses in Table 3). One possible explanation for this discrepancy is that geometric and loading imperfections are not accounted for in the linearized buckling analyses, and that the imperfection sensitivity driven by unstable cylinder buckling has led to a knockdown in observed buckling load. This explanation is not considered to be likely for two reasons. First, the pristine versions of Shell A and Shell B (without cutouts) were previously shown to be

insensitive to imperfections [51], with good correlations between linearized buckling analyses and test results. Second, the buckling load predictions of the nonlinear dynamic analyses, which follow in the next section, correlate closely with the experimental test results and also do not account for geometric/loading imperfections. The discrepancy between linear global buckling load prediction and global buckling test results likely stems from the linearization of the model around a prebuckling state prior to the occurrence of local buckling. As is shown in the following section, the onset of local buckling around the cutouts is a stable buckling event (akin to plate buckling) whereby the cylinder retains significant, yet slightly reduced ($\approx -5\%$) postcritical axial stiffness. Hence, the geometric nonlinearity induced by the first local buckling event leads to an overestimation of higher-order buckling loads in the linearized eigenvalue analysis.

B. Nonlinear Dynamic Analysis

The loading-unloading cycle of the nonlinear dynamic analysis conducted in ABAQUS 2018 for Shell A-Small, Shell B-Small, Shell A-Large, and Shell B-Large alongside their experimental test results are shown in the end-shortening *vs* reaction force plots of Figs 6a, 7a, 8a and 9a, respectively. Radial displacements from ABAQUS 2018 and radial displacements measured using DIC in the experiments are shown as color contours (blue=inwards and red=outwards) in Figs 6b, 7b, 8b and 9b. In each end-shortening *vs* reaction force equilibrium plot, the axially-compressed cylinder follows a practically linear prebuckling path until global buckling occurs with a concomitant drop in the reaction force. Hence, the prebuckling equilibrium path loses stability, and the cylinders dynamically transition into a new stable equilibrium of lower reaction force for the same value of applied end-shortening. To mimic the experimental tests, the end-shortening is then reversed after buckling, such that the cylinders follow a different equilibrium path upon unloading, until the cylinders reconnect to the prebuckling equilibrium path at a lower reaction force than the global buckling load (hysteresis).

As is apparent from the plots, the prebuckling stiffness along the prebuckling path is accurately captured by the FE model. After an initial portion of loading that presumably removes "slack" in the testing system, the prebuckling curves from the FE model and the experimental results are indistinguishable. This is noteworthy as apart from extending the boundary conditions in the model to encompass the potted end regions, no other modifications to the potting region stiffness (as is often done in the literature [32, 56]) were embedded in the model. For the FE model, the equilibrium paths in the prebuckling regime are coincident throughout the loading and unloading cycles, while for the experiments, the equilibrium path is shifted to a lower reaction force for the same level of end-shortening. As the overall slope of the curve, and hence the structural stiffness, remains unchanged, this is likely to have been caused by small movements in the testing frame as a result of the dynamic buckling event.

As summarized in Table 4, the global buckling prediction of all four FE models correlates closely with the experimental test result (within 3.5%). This is noteworthy as no geometric imperfections or loading eccentricities were incorporated in the model, suggesting that the cylinder designs are insensitive to imperfections. As discussed

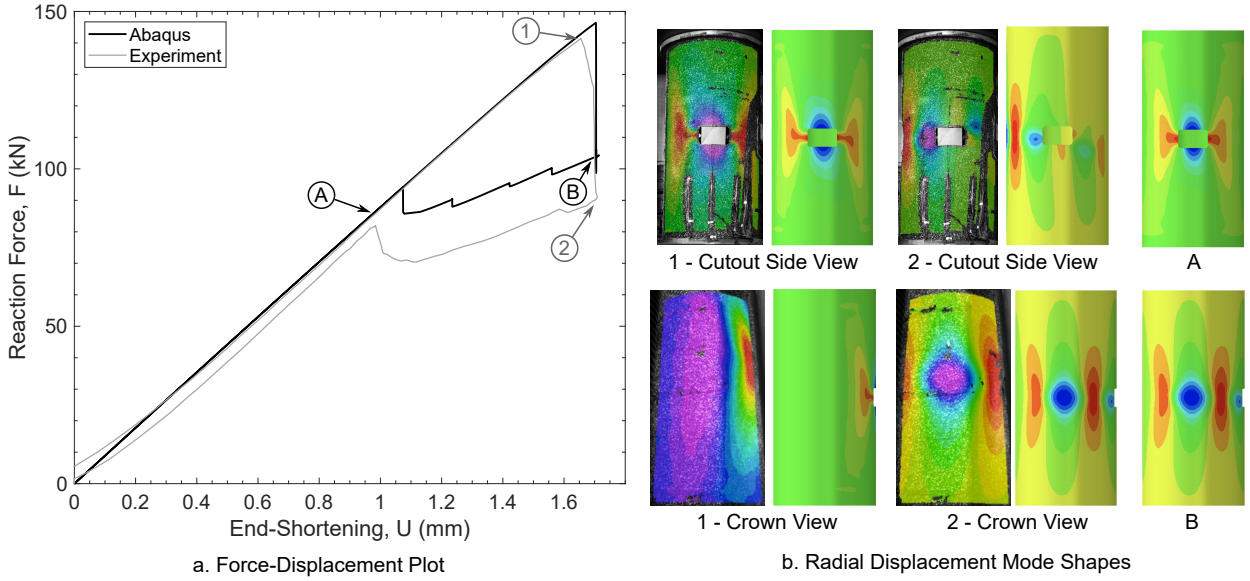

Fig. 6 Shell A-Small: (a) End-shortening *vs* reaction force plot with a comparison of FE results and experimental test measurements. The points highlighted on the equilibrium plot correspond to the deformation mode shapes shown in (b) that compare the radial displacements extracted from ABAQUS 2018 with the DIC measurements taken from the experiments. Red/blue colors denote displacements that are radially outwards/inwards, respectively.

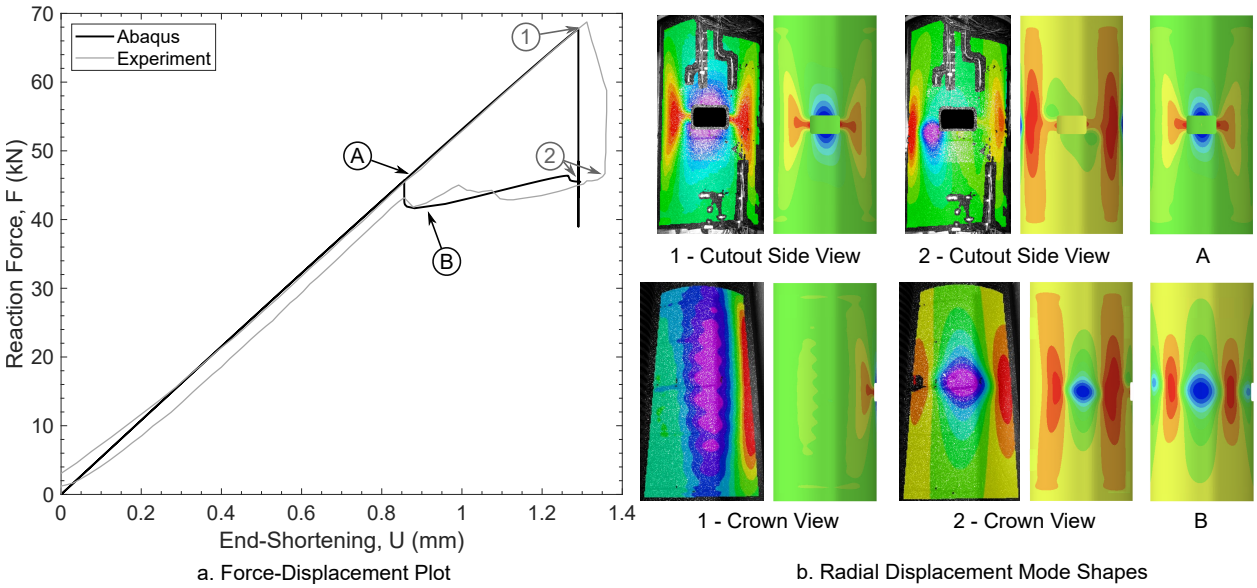

Fig. 7 Shell B-Small: (a) End-shortening *vs* reaction force plot with a comparison of FE results and experimental test measurements. The points highlighted on the equilibrium plot correspond to the deformation mode shapes shown in (b) that compare the radial displacements extracted from ABAQUS 2018 with the DIC measurements taken from the experiments. Red/blue colors denote displacements that are radially outwards/inwards, respectively.

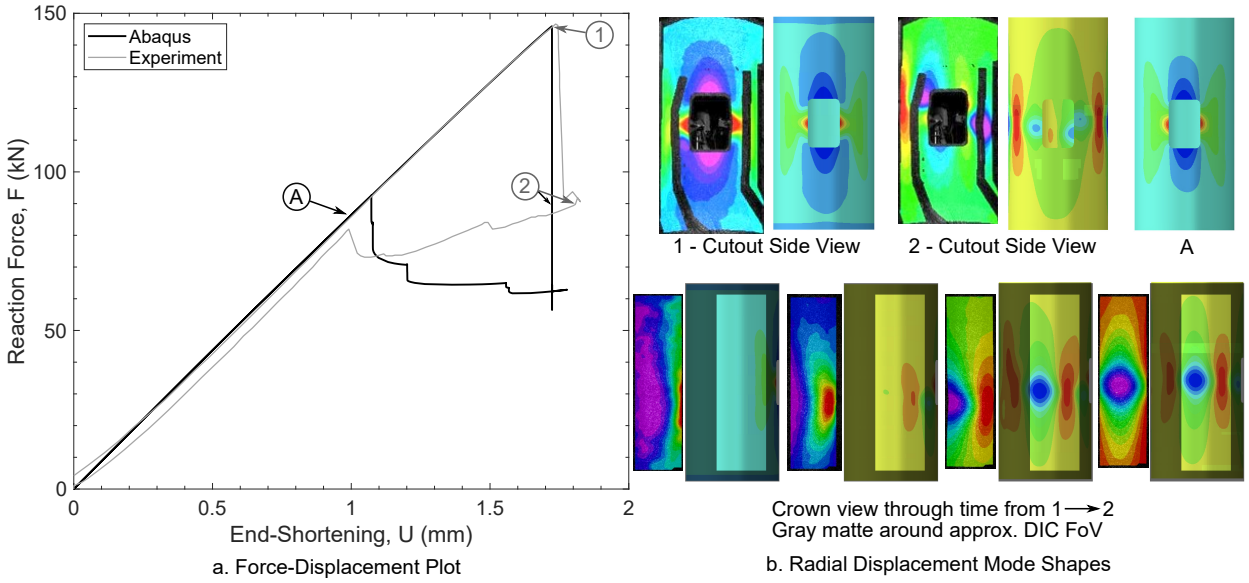

Fig. 8 Shell A-Large: (a) End-shortening *vs* reaction force plot with a comparison of FE results and experimental test measurements. The points highlighted on the equilibrium plot correspond to the deformation mode shapes shown in (b) that compare the radial displacements extracted from ABAQUS 2018 with the DIC measurements taken from the experiments. Red/blue colors denote displacements that are radially outwards/inwards, respectively. Gray matte area on deformation snap shots shows the approximate DIC field of view.

elsewhere [35], one explanation for this phenomenon is that the nonuniform stiffness distribution, and in this case also the presence of a cutout, breaks the otherwise symmetric prebuckling membrane stress field, such that imperfections only play an important role in highly-stressed regions, which form a small subset of the total cylinder geometry. Similarly, buckling of symmetric structures is usually associated with breaking of symmetry groups [57], and the high number of almost-coincident eigenvalues uncovered in linear and nonlinear eigenvalue analyses of axially-compressed cylinders [58, 59] is testament to the large number of symmetry groups that can be broken as the fundamental state of axial compression and circumferential dilation loses stability. It is well known that this scenario of multiple coincident buckling modes leads to the phenomenon of *mode interaction* and unstable buckling. By breaking the otherwise geometrically perfect and materially isotropic cylinder using tow-steered stiffness tailoring, a smaller subset of symmetry groups can be broken during the instability event, such that geometric or loading imperfections are less likely to break these symmetry groups spontaneously, which then leads to a discrepancy between model prediction and testing result.

Table 4 also compares the restabilized postbuckling reaction force of the FE models to the test results. For three cylinders out of the four tested, the FE model under-predicts the load carried by the cylinders after buckling. For Shell B-Small this under-prediction is negligibly small (2.6%), whereas for the other two cylinders (Shell A-Large and Shell B-Large) the discrepancy is greater (30% & 17%). This means that upon buckling, Shell A-Large and Shell B-Large traversed further down the load-displacement plot to a restabilized equilibrium of lower strain energy than observed in the tests. This discrepancy is not uncommon in dynamic analyses (see, *e.g.*, Ref. [32]), and can be attributed to

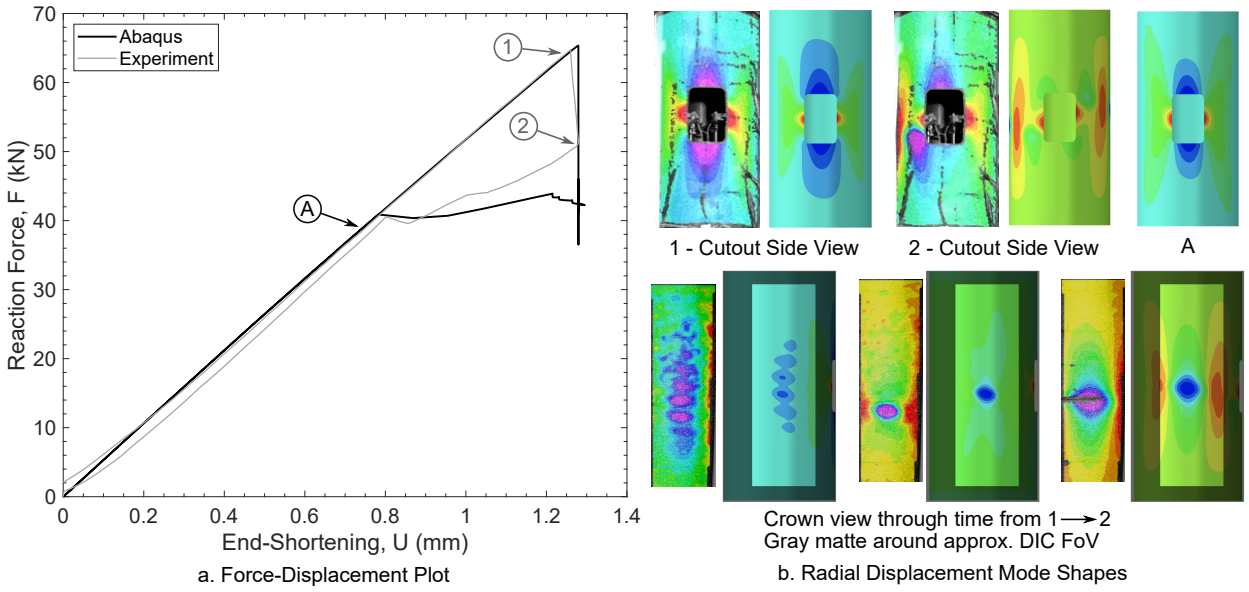

Fig. 9 Shell B-Large: (a) End-shortening *vs* reaction force plot with a comparison of FE results and experimental test measurements. The points highlighted on the equilibrium plot correspond to the deformation mode shapes shown in (b) that compare the radial displacements extracted from ABAQUS 2018 with the DIC measurements taken from the experiments. Red/blue colors denote displacements that are radially outwards/inwards, respectively. Gray matte area on deformation snap shots shows the approximate DIC field of view.

additional restraints and friction between the testing apparatus and the specimen, or even to deformation within the test platens. Essentially, the cylinder/test-frame assembly stores excess potential energy when compared to the FE model, thereby restabilizing the cylinder in a local energy well of higher potential (corresponding to greater reaction force under displacement-controlled loading). Indeed, friction and "free play" in the testing system are likely explanations for the discrepancies observed, as the experimental prebuckling path itself shows signs of hysteretic behavior. Furthermore, for some test specimens, the dynamic mode change upon buckling is less sudden than expected (see, *e.g.*, the non-vertical load-displacement curve of Figs 6a and 7a), suggesting that the energy released upon buckling is partially dissipated rather than being fully converted into kinetic energy to traverse dynamically across local energy minima in the energy landscape. The FE model could be improved by incorporating these effects or tailoring the damping coefficients in the HHT algorithm [55].

Despite this difference in restabilized reaction force and the ensuing differences in the unloading equilibrium path of Figs 6a, 7a, 8a and 9a, the overall postbuckling deformation modes are captured accurately by the FE model from both crown and cutout side views, as shown in Figs 6b, 7b, 8b and 9b. Furthermore, the reconnections to the prebuckling paths in Figs 6a, 7a, 8a and 9a as the cylinders are unloaded is accurately represented, occurring at similar levels of end-shortening and reaction force, and either occurring as a sudden snap (sharp vertical line) or more gradually.

In all cases, the mode shape just prior to global buckling (point 1) is characterized by deformations around the cutout that relate to the prior onset of local buckling (see point A) that was discussed in the previous section. Indeed, point A in

Table 4 Nonlinear buckling load and restabilized postbuckling load predictions from an implicit dynamic analysis in ABAQUS 2018. Percentage difference to experimental values shown in parentheses.

Load	Shell A		Shell B	
	Small	Large	Small	Large
Global Buckling (kN)	146.3 (3.5%)	145.9 (-0.61%)	67.6 (-1.9%)	65.4 (0.68%)
Restabilized Postbuckling (kN)	104.3 (15%)	62.8 (-30%)	45.5 (-2.6%)	42.2 (-17%)

Figs 6a, 7a, 8a and 9a denotes the equilibrium state for a load level just greater than the local buckling load predicted by the linearized eigenvalue analysis. The corresponding mode shapes for point A in Figs 6b, 7b, 8b and 9b show that the cylinder has transitioned onto another stable postcritical path with radial deformations localized around the cutouts. For all cases, there is a small reduction in the axial stiffness of $\approx$ 5%–10% once local buckling occurs. Hence, the linearized eigenvalue analysis provides a correct first-order approximation of the stability behavior in that local buckling around the cutout is followed by global buckling on the crown and keel of the cylinder. Fig. 10a shows force-displacement curves for axial end-shortening *vs* axial reaction force and curves for local radial displacement around the cutout *vs* the same axial reaction force, both for Shell B-Large. The reduction in slope of the radial displacement curve (blue) in the vicinity of the local buckling load (predicted by the linearized eigenvalue analysis) is indicative of local buckling around the cutout. However, the onset of local buckling does not lead to a pronounced reduction in global axial stiffness (slope of the end-shortening *vs* reaction force curve in black). This observation is shown more clearly in Fig. 10b, which shows a relatively small drop in tangential axial stiffness (computed as the ratio of the change in reaction force *vs* change in end-shortening between two consecutive data points) for Shell B-Large when local buckling occurs around the cutout, and a much larger drop towards global buckling. A comparison with the tangent axial stiffness of Shell B *without* cutouts (blue line in Fig. 10b), for which local buckling around a cutout does not occur, further highlights the slight reduction in axial stiffness due to local buckling around the large cutout.

The reason for the relatively small reduction in structural stiffness beyond local buckling is that stiffness tailoring due to tow steering has already redistributed the axial membrane forces away from the cutout to the crown/keel regions before local buckling has occurred. Thus, as the local buckling mode develops around the cutout, the ensuing redistribution of loads away from the buckled region is negligibly small compared to the prior load redistribution due to stiffness tailoring. This is shown explicitly for Shell B-Large in Fig. 10c–d, where prior to buckling, the compressive axial stress resultant is already concentrated away from the cutout on the crown/keel regions (see Fig. 10c) due to the greater axial stiffness in these regions. As a result, the membrane stress distribution prior to local buckling (Fig. 10c) already mimics the stress distribution that occurs after local buckling around the cutouts (Fig. 10d), and therefore local buckling does not significantly impact the structural response. Akin to the mechanics observed in the buckling of tow-steered flat plates [26], the redistribution of compressive stresses away from unsupported regions by means of tow steering can lead to behavior that is more stable and even "buckle free" [26]. Hence, apart from minimizing stress concentrations around

cutouts, tow steering is also useful for improving the stability of thin-walled structures with cutouts. In this manner, the sizing of typical stiffening elements, such as discrete circumferential hoops or axial stringers, can be reduced and therefore lead to further lightweighting.

What cannot be accurately determined from the linearized buckling analysis are the restabilized postbuckling modes. While the linear eigenmodes in Fig. 5 suggest a periodic wavefront along the cylinder axis in the crown/keel regions, the nonlinear postbuckling modes (see point 2 in Figs 6, 7, 8, and 9) feature a single large inward diamond-shaped buckle in the crown/keel regions surrounded by smaller outward crests to the left and right (circumferential direction) of the single diamond buckles. Indeed, cylinder buckling is prone to spatial localization, whereby isolated buckles can readily form along the cylinder length and then multiply circumferentially in a phenomenon known as *homoclinic snaking* or *cellular buckling* [58, 59]. Returning to the analogy of the beam on an elastic foundation, even this simple 1D system is prone to buckling-mode localization if the elastic foundation is defined to be of the nonlinear softening-stiffening type. In this case, the linear eigenmode is periodic and envelops the entire beam length, but immediately and dynamically localizes in one position along the beam length as buckling is initiated at a subcritical bifurcation. Indeed, if the circumferential hoop stiffness of the cylinder is taken to act as an elastic foundation, then the effective stiffness of this foundation can be shown to be of the softening-stiffening type beyond a certain level of axial compression [60]. Particularly for Shell B-Large in Fig. 9b, we observe this precise dynamic sequence, where the radial deformation mode from point 1 to point 2 first shows a trace of the linear buckling mode in the crown region, which then dynamically localizes along the length to form a single buckle.

C. Deep Postbuckling Analysis

The tow-steered shells with small and large cutouts were only tested to global buckling, as described in Refs [52, 53], and these experimental results were compared to nonlinear dynamic FE analyses in the preceding sections. While these shells were not loaded into the deep postbuckling regime during the experimental tests, their predicted response to additional end-shortening is now simulated using the same Abaqus geometrically nonlinear FE models. In particular, dynamic mode changes in the deep postbuckling regime are of interest. These computational predictions—while not experimentally validated—are presented and discussed to provide additional insight into the tow-steered shells' deep postbuckling behavior in the presence of cutouts of different sizes. To provide a baseline for comparison, the deep postbuckling behaviors of the pristine Shell A and pristine Shell B without cutouts, previously presented by White *et al.* [32], are also presented. These analytical results in [32] are in overall very good agreement with the corresponding experimental data in [31]. This correlation gives added confidence in the validity of the simulations presented here.

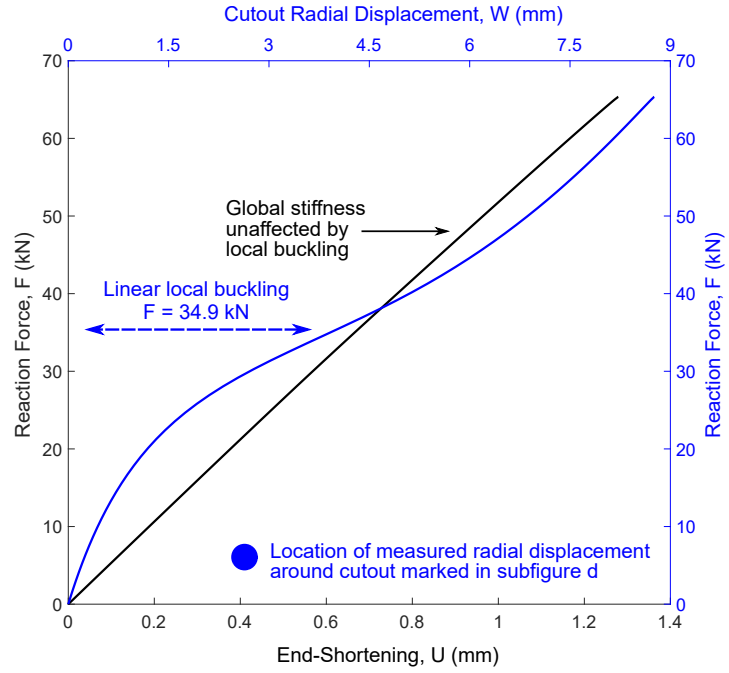

a. Shell B-Large: Force-Displacement Plot

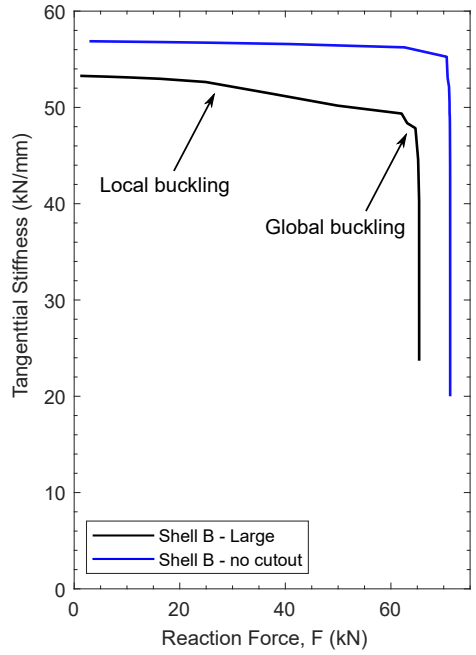

b. Shell B-Large: Tangential Stiffness Plot

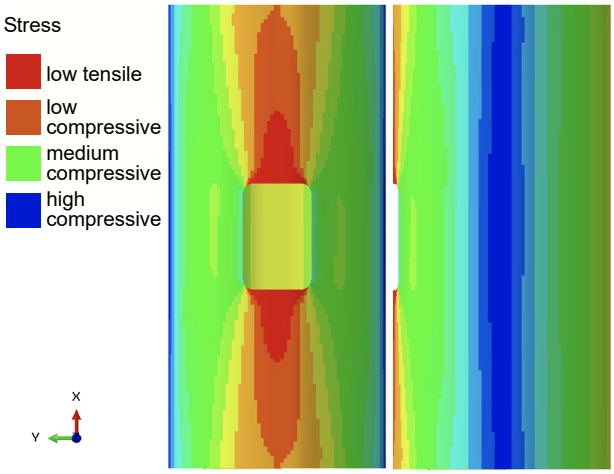

c. Shell B-Large: F = 1 kN

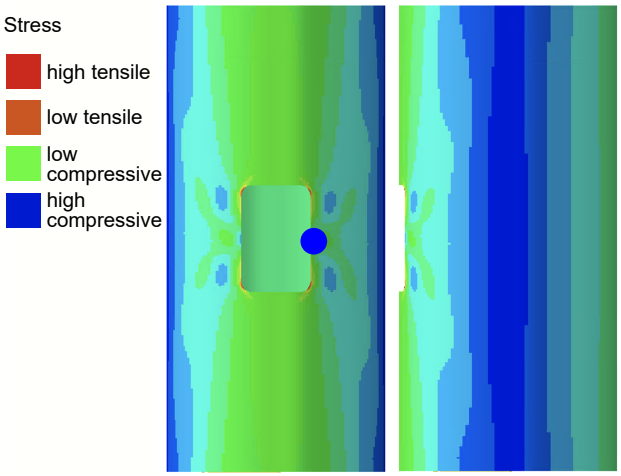

d. Shell B-Large: F = 62 kN

Fig. 10 (a) Force-displacement plot for Shell B-Large showing both end-shortening (U) and radial displacement around the cutout (W) *vs* the measured reaction force (F). Plot (b) compares the tangent axial stiffness of Shell B-Large with Shell B without cutouts. A small drop in stiffness at local buckling around the large cutout is observed. Axial membrane stress resultant for Shell B-Large (c) before local buckling around the cutout (reaction force $F = 1.11$ kN), and (d) after local buckling (reaction force $F = 62.3$ kN). Blue contours denote high-magnitude compressive stress.

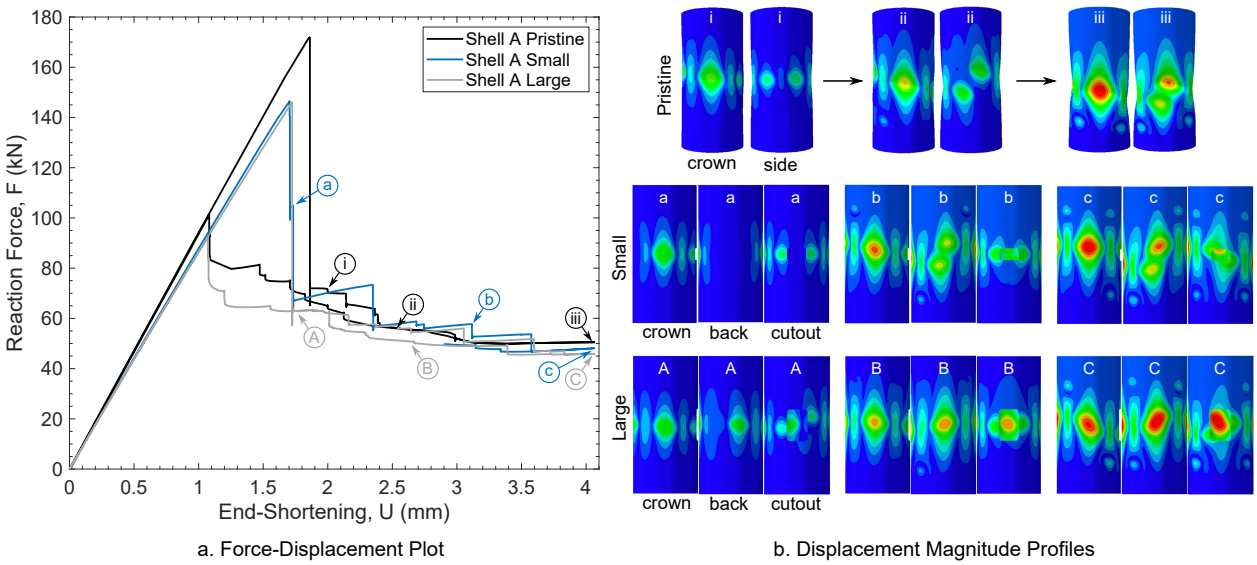

a. Force-Displacement Plot

b. Displacement Magnitude Profiles

Fig. 11 (a) Force-displacement plot for Shell A without cutouts (pristine) and with small and large cutouts into the deep postbuckling regime showing a number of load drops corresponding to mode changes. The displacement magnitude profiles in (b) qualitatively show the buckling mode progression up to the maximum applied end-shortening.

1. Shell A (shell with tow overlaps)

Figure 11 shows the predicted load *vs* end-shortening curves of Shell A-Pristine and Shell A with small and large cutouts into the deep postbuckling regime. It is apparent by the number of load drops that with increasing end-shortening the buckling mode shape changes on several occasions. It is interesting to note that the curves for Shell A-Pristine and Shell A-Large continuously slope downwards, while Shell A-Small initially recovers positive postbuckling stiffness that is then degraded in a sequence of additional load drops. At the maximum applied end-shortening of 4.064 mm all shells have effectively reached a plateau of near-zero postbuckling stiffness. Interestingly, throughout the computed postbuckling regime, the load *vs* end-shortening curves of all three shells fall within the same approximate region, suggesting that the postbuckling load-carrying capacity of Shell A is not strongly affected by either the presence or the size of the cutouts.

In terms of the mode shapes, Shell A-Pristine (top row of Fig. 11b) first buckles by developing a single deep dimple oriented radially inwards and centered on the shell mid-length on both the crown and keel. Two shallower dimples also form on either side of the crown and keel at the cylinder's mid-length. As the shell is loaded into deep postbuckling, these two dimples near the shell's side move both closer together and also asymmetrically towards opposite ends of the cylinder. The amplitudes of their radial deflections also increase, until finally the two dimples start to coalesce into a single elongated diagonal dimple with two local minima. For Shell A-Small (middle row of Fig. 11b), the global buckling event is again characterized by the rapid growth of large inward radial buckles that are centered on the shell crown and keel. During the second localized buckling event that follows immediately afterward, these radial

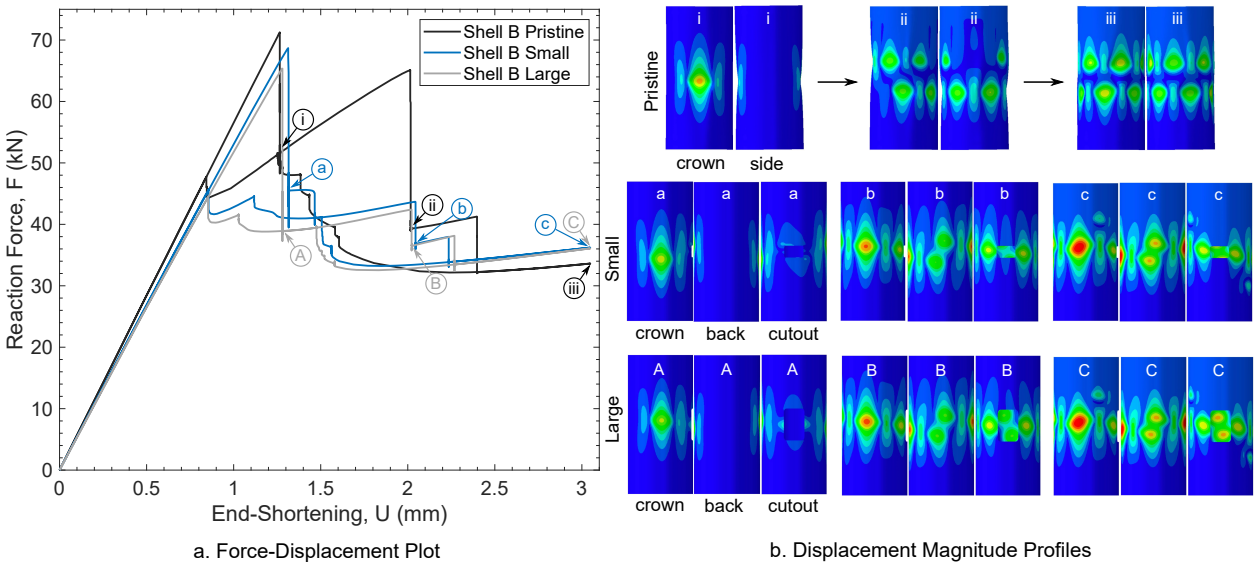

a. Force-Displacement Plot

b. Displacement Magnitude Profiles

Fig. 12 (a) Force-displacement plot for Shell B without cutouts (pristine) and with small and large cutouts into the deep postbuckling regime showing a number of load drops corresponding to mode changes. The displacement magnitude profiles in (b) qualitatively show the buckling mode progression up to the maximum applied end-shortening.

deformations on the shell crown and keel increase, and radial deformations appear on either side of the cutout. For the third and final localized buckling event, two asymmetric radial deformations—located above and below (axial direction) the shell mid-plane—form and coalesce on the back side of the shell opposite the cutout*. Shell A-Large (bottom row of Fig. 11b) exhibits fewer localized buckling events than Shell A-Small. The initiation of buckling is similar with a pronounced inwards dimple on the crown and keel, followed by the addition of buckles around the cutout and on the back side of the shell. Compared to Shell A-Small, the buckle on the back side shows one large skewed buckle rather than two coalescing dimples on a diagonal.

2. Shell B (without tow overlaps)

Figure 12 shows the load *vs* end-shortening curves of Shell B-Pristine and Shell B with small and large cutouts into the deep postbuckling regime. Shell B-Pristine restabilizes after the initial global buckling event and continues to take load at a positive, albeit reduced, stiffness. This restabilized postbuckling mode corresponds to a large single buckle on both the crown and keel (top row of Fig. 12b), and the applied load in this secondary buckling mode almost reaches the buckling load of the initial instability. Upon further compression up to the maximum applied end-shortening (3.048 mm), Shell B-Pristine loses stability again, and the associated load drop corresponds to a mode change to an asymmetric two-tier diamond pattern of circumferential buckles with six radially inwards buckles separated by six outwards crests in each tier.

*Note, Shell A-Small did not complete the unloading sequence in Abaqus owing to convergence problems. The cause of this is unknown and did not occur for any other Shell A or Shell B analyzed herein. This is, however, not significant in terms of interpreting the results presented.

Compared to Shell A, the presence of cutouts in Shell B affects the deep postbuckling response more strongly when compared to the pristine version of the shells. Both Shells B-Small and -Large show a significant load drop upon buckling and restabilization at a much lower load than Shell B-Pristine. While the introduction of the cutout clearly influences the load *vs* end-shortening response, the difference in behavior between the small and large cutouts is negligible, with almost identical equilibrium paths throughout the loading history. Furthermore, the postbuckling mode shapes of Shells B-Small and -Large (middle and bottom rows of Fig. 12b, respectively) are much closer to those of Shells A-Small and -Large than those of Shells B-Pristine and A-Pristine. As was observed for Shells A-Small and -Large, Shells B-Small and -Large first buckle on the crown and keel and then develop an asymmetric pair of buckles on the back side opposite to the cutout. Upon initially buckling on the crown and keel, the shells redistribute internal loads to the surrounding unbuckled areas. For the shells with cutouts the only unbuckled area, or region with load-carrying material, is the back side opposite to the cutout. Hence, the postbuckling behaviors of all shells with cutouts should be similar as they follow the progression of buckling on crown/keel (highest loaded region pre global buckling) followed by buckling on the back side (highest loaded region post global buckling).

For the pristine shells, both sides adjacent to the crown/keel can act as load attractors upon global buckling. The difference between Shell A-Pristine and Shell B-Pristine is that, upon first buckling, the latter shell restabilizes into a postbuckled deformation pattern with a positive-stiffness load *vs* end-shortening response. Indeed, for Shell B-Pristine the buckle on the crown and keel is slightly smaller than for Shell A-Pristine. Therefore, Shell B-Pristine retains greater load-carrying capacity upon first buckling (smaller load drop and restabilized positive stiffness), because the internal load can be redistributed to a greater proportion of an unbuckled shell circumference. In the case of the shells with cutouts, this load redistribution is precluded due to the presence of a cutout on one side and hence all shells with cutouts (Shells A-Small and -Large, and Shells B-Small and -Large) show large load drops upon buckling.

A key consideration for designing cylinders with favorable postbuckling stiffness is to restrict buckle formation to as small an area as possible. This could, for example, be achieved by more aggressive and local steering over a smaller circumferential portion with straight-fiber layups in-between. For the present shell design, this would correspond to a larger proportion of ±45 degree plies around the circumference with only local steering to ±10 degree plies on the crown and keel. A key consideration is that the regions of axially aligned fibers (±10 degree) should provide increased membrane stiffness to attract load in the prebuckling regime, whilst not unduly increasing the local bending stiffness (*e.g.* through overlaps or increased thickness) that would resist short-wavelength buckle formation.

VI. Conclusion

In conclusion, the nonlinear dynamic results discussed herein provide significant physical insight into the buckling and postbuckling response of tow-steered cylinders with cutouts. Most importantly, tow steering facilitates a redistribution of compressive stresses away from unsupported regions (the cutouts) such that local buckling events around the cutout

do not significantly affect the postcritical structural response. Global buckling itself—as a secondary event after primary buckling around the cutouts—is then initiated in the axially-stiff crown/keel regions, and the concomitant reduction in load-carrying capacity occurs as no further load redistributions to other parts of the cylinder are possible once the crown/keel regions have buckled. In this regard, linearized buckling analyses provide a good first-order approximation of the primary local buckling event around the cutouts, and provide acceptable accuracy in predicting the subsequent global buckling event. The accuracy in predicting the global buckling event could be improved at little computational expense by conducting a linearized buckling analysis based on a converged stress state after the first local instability around the cutouts has occurred.

As is typical of cylinder buckling, the global buckling mode predicted by the linearized analysis has no bearing on the actual restabilized postbuckling mode observed in practice due to the strong mode interaction and proclivity for axial and circumferential localization. Following previous observations on cylinders without cutouts [58, 59], the single diamond-shaped buckle in the crown/keel regions of the tow-steered cylinders, observed both in the FE models and in the experiments, is likely to multiply circumferentially or transition into a two-tier pattern as end-shortening is increased beyond the values studied here. Overall, the present work expands the current state of knowledge on tow-steered cylinders, and showcases the benefit of ameliorating some of the adverse structural effects associated with cutouts. In the authors' opinion, tow-steered composites have great potential to steer the way towards a new generation of high-performance and lightweight aerospace structures.

Acknowledgments

R.M.J.G. acknowledges the support and funding of the Royal Academy of Engineering under the Research Fellowship scheme [RF\201718\17178].

References

[1] Groh, R. M. J., and Wu, C. K., "Nonlinear Buckling Analysis of Tow-Steered Composite Cylinders with Cutouts," *AIAA SciTech 2022 Forum and Exposition*, 2022. https://doi.org/10.2514/6.2022-2148, Paper Nr. 2022-2148.

[2] Hilburger, M. W., and Starnes Jr., J. H., "Buckling Behavior of Compression-Loaded Composite Cylindrical Shells with Reinforced Cutouts," *International Journal of Nonlinear Mechanics*, Vol. 43, 2005, pp. 1005–1021. https://doi.org/10.1016/j.ijnonlinmec.2005.02.001.

[3] Zappino, E., Filippi, M., Pagani, A., Petiti, M., and Carrera, E., "Experimental and Numerical Analysis of 3D Printed Open-Hole Plates Reinforced with Carbon Fibers," *Composites Part C: Open Access*, Vol. 2, 2020, p. 100007. https://doi.org/10.1016/j.jcomc.2020.100007.

[4] Almeida Jr, J. H. S., Bittrich, L., and Spickenheuer, A., "Improving the open-hole tension characteristics with variable-axial

composite laminates: Optimization, progressive damage modeling and experimental observations," *Composites Science and Technology*, Vol. 185, 2020, p. 107889. https://doi.org/10.1016/j.compscitech.2019.107889.

[5] Jegley, D. C., Tatting, B. F., and Gürdal, Z., "Optimization of Elastically Tailored Tow-Placed Plates with Holes," *Proceedings of the 44th AIAA/ASME/ASCE/AHS/ASC Structures, Structural Dynamics and Materials Conference*, Norfolk, VA, USA, 2013. https://doi.org/10.2514/6.2003-1420, Paper Nr. 2003-1420.

[6] Jegley, D. C., Tatting, B. F., and Gürdal, Z., "Tow-Steered Panels with Holes Subjected to Compression or Shear Loading," *Proceedings of the 46th AIAA/ASME/ASCE/AHS/ASC Structures, Structural Dynamics and Materials Conference*, Austin, TX, USA, 2013. https://doi.org/10.2514/6.2005-2081, Paper Nr. 2005-2081.

[7] Lukaszewicz, D. H.-J. A., Ward, C., and Potter, K. D., "The Engineering Aspects of Automated Prepreg Layup: History, Present and Future," *Composites Part B: Engineering*, Vol. 43, No. 3, 2012, pp. 997–1009. https://doi.org/10.1016/j.compositesb.2011.12.003.

[8] Kim, B. C., Potter, K. D., and Weaver, P. M., "Continuous Tow Shearing for Manufacturing Variable Angle Tow Composites," *Composites: Part A*, Vol. 43, 2012, pp. 1347–1356. https://doi.org/10.1016/j.compositesa.2012.02.024.

[9] Almeida Jr, J. H. S., St-Pierre, L., Wang, Z., Ribeiro, M. L., Tita, V., Amico, S. C., and Castro, S. G. P., "Design, modeling, optimization, manufacturing and testing of variable-angle filament-wound cylinders," *Composites Part B: Engineering*, Vol. 225, 2021, p. 109224. https://doi.org/10.1016/j.compositesb.2021.109224.

[10] Ribeiro, P., Akhavan, H., Teter, A., and Warminski, J., "A Review on the Mechanical Behaviour of Curvilinear Fibre Composite Laminated Panels," *Journal of Composite Materials*, Vol. 48, No. 22, 2014, pp. 2761–2777. https://doi.org/10.1177/0021998313502066.

[11] Lopes, C. S., Gürdal, Z., and Camanho, P. P., "Tailoring for Strength of Composite Steered-Fibre Panels with Cutouts," *Composites Part A: Applied Science and Manufacturing*, Vol. 41, 2010, pp. 1760–1767. https://doi.org/10.1016/j.compositesa.2010.08.011.

[12] Zucco, G., Rouhi, M., Oliveri, V., Cosentino, E., O'Higgins, R. M., and Weaver, P. M., "Continuous Tow Steering Around an Elliptical Cut-Out in a Composite Panel," *AIAA SciTech 2021 Forum and Exposition*, 2021. https://doi.org/10.2514/6.2021-0918, Paper Nr. 2021-0918.

[13] Janssens, T. A., and Castro, S. G. P., "Semi-Analytical Modelling of Variable Stiffness Laminates with Discontinuities," *AIAA SciTech 2021 Forum and Exposition*, 2021. https://doi.org/10.2514/6.2021-0440, Paper Nr. 2021-0440.

[14] Gürdal, Z., Tatting, B. F., and Wu, K. C., "Variable Stiffness Composite Panels: Effects of Stiffness Variation on the In-Plane and Buckling Response," *Composites Part A: Applied Science and Manufacturing*, Vol. 39, 2008, pp. 911–922. https://doi.org/10.1016/j.compositesa.2007.11.015.

[15] Setoodeh, S., Abdalla, M. M., Ijsselmuiden, S. T., and Gürdal, Z., "Design of Variable Stiffness Composite Panels for Maximum Buckling Load," *Composite Structures*, Vol. 87, 2008, pp. 109–117. https://doi.org/10.1016/j.compstruct.2008.01.008.

[16] Alhajahmad, A., Abdalla, M. M., and Gürdal, Z., "Optimal Design of Tow-Placed Fuselage Panels for Maximum Strength with Buckling Considerations," *Journal of Aircraft*, Vol. 47, No. 3, 2010, pp. 775–782. https://doi.org/10.2514/1.40357.

[17] Wu, Z., Weaver, P. M., Raju, G., and Kim, B. C., "Buckling Analysis and Optimisation of Variable Angle Tow Composite Plates," *Thin-Walled Structures*, Vol. 60, 2012, pp. 163–172. https://doi.org/10.1016/j.tws.2012.07.008.

[18] Raju, G., Wu, Z., Kim, B. C., and Weaver, P. M., "Prebuckling and Buckling Analysis of Variable Angle Tow Plates with General Boundary Conditions," *Composite Structures*, Vol. 94, No. 9, 2012, pp. 2961–2970. https://doi.org/10.1016/j.compstruct.2012.04.002.

[19] Wu, Z., Raju, G., and Weaver, P. M., "Postbuckling Analysis of Variable Angle Tow Composite Plates," *International Journal of Solids and Structures*, Vol. 50, 2013, pp. 1770–1780. https://doi.org/10.1016/j.ijsolstr.2013.02.001.

[20] Wu, Z., Weaver, P. M., and Raju, G., "Postbuckling Optimisation of Variable Angle Tow Composite Plates," *Composite Structures*, Vol. 103, 2013, pp. 34–42. https://doi.org/10.1016/j.compstruct.2013.03.004.

[21] White, S. C., Raju, G., and Weaver, P. M., "Initial Post-Buckling of Variable-Stiffness Curved Panels," *Journal of the Mechanics and Physics of Solids*, Vol. 71, 2014, pp. 132–155. https://doi.org/10.1016/j.jmps.2014.07.003.

[22] Groh, R. M. J., and Weaver, P. M., "Mass Optimization of Variable Angle Tow, Variable Thickness Panels with Static Failure and Buckling Constraints," *AIAA SciTech 2015 Forum and Exposition*, 2015. https://doi.org/10.2514/6.2015-0452, Paper Nr. 2015-0452.

[23] Zucco, G., Groh, R. M. J., Madeo, A., and Weaver, P. M., "Mixed Shell Element for Static and Buckling Analysis of Variable Angle Tow Composite Plates," *Composite Structures*, Vol. 152, 2016, pp. 324–338. https://doi.org/10.1016/j.compstruct.2016.05.030.

[24] White, S. C., and Weaver, P. M., "Towards Imperfection Insensitive Buckling Response of Shell Structures-Shells with Plate-Like Post-Buckled Responses," *Aeronautical Journal*, Vol. 120, No. 1224, 2016, pp. 233–253. https://doi.org/10.1017/aer.2015.14.

[25] Madeo, A., Groh, R. M. J., Zucco, G., Weaver, P. M., Zagari, G., and Zinno, R., "Post-Buckling Analysis of Variable-Angle Tow Composite Plates Using Koiter's Approach and the Finite Element Method," *Thin-Walled Structures*, Vol. 110, 2017, pp. 1–13. https://doi.org/10.1016/j.tws.2016.10.012.

[26] Wu, Z., Raju, G., and Weaver, P. M., "Optimization of Postbuckling Behaviour of Variable Thickness Composite Panels with Variable Angle Tows: Towards "Buckle-Free" Design Concept," *International Journal of Solids and Structures*, Vol. 132-133, 2018, pp. 66–79. https://doi.org/10.1016/j.ijsolstr.2017.08.037.

[27] Zucco, G., and Weaver, P. M., "Post-Buckling Behaviour in Variable Stiffness Cylindrical Panels Under Compression Loading with Modal Interaction Effects," *International Journal of Solids and Structures*, Vol. 203, 2020, pp. 92–109. https://doi.org/10.1016/j.ijsolstr.2020.06.025.

[28] Daghighi, S., Zucco, G., Rouhi, M., and Weaver, P. M., "Bend-Free Design of Super Ellipsoids of Revolution Composite Pressure Vessels," *Composite Structures*, Vol. 245, 2020, p. 112283. https://doi.org/10.1016/j.compstruct.2020.112283.

[29] Daghighi, S., and Weaver, P. M., "Three-Dimensional Effects Influencing Failure in Bend-Free, Variable Stiffness Composite Pressure Vessels," *Composite Structures*, Vol. 262, 2021, p. 113346. https://doi.org/10.1016/j.compstruct.2020.113346.

[30] Blom, A. W., Stickler, P. B., and Gürdal, Z., "Optimization of a Composite Cylinder Under Bending by Tailoring Stiffness Properties in Circumferential Direction," *Composites: Part B*, Vol. 41, 2010, pp. 157–165. https://doi.org/10.1016/j.compositesb.2009.10.004.

[31] Wu, K. C., Stanford, B. K., Hrinda, G. A., Wang, Z., Martin, R. A., and Kim, H. A., "Structural Assessment of Advanced Composite Tow-Steered Shells," *Proceedings of the 54th AIAA/ASME/ASCE/AHS/ASC Structures, Structural Dynamics and Materials Conference*, Boston, MA, USA, 2013. https://doi.org/10.2514/6.2013-1769, Paper Nr. 2013-1769.

[32] White, S. C., Weaver, P. M., and Wu, K. C., "Post-Buckling Analyses of Variable-Stiffness Composite Cylinders in Axial Compression," *Composite Structures*, Vol. 123, 2015, pp. 190–203. https://doi.org/10.1016/j.compstruct.2014.12.013.

[33] Labans, E., and Bisagni, C., "Buckling and Free Vibration Study of Variable and Constant-Stiffness Cylindrical Shells," *Composite Structures*, Vol. 210, 2019, pp. 446–457. https://doi.org/10.1016/j.compstruct.2018.11.061.

[34] Wang, Z., Almeida Jr., J. H. S., St-Pierre, L., Wang, Z., and Castro, S. G. P., "Reliability-Based Buckling Optimization with an Accelerated Kriging Metamodel for Filament-Wound Variable Angle Tow Composite Cylinders," *Composite Structures*, Vol. 254, 2020, p. 112821. https://doi.org/10.1016/j.compstruct.2020.112821.

[35] Lincoln, R. L., Weaver, P. M., Pirrera, A., and Groh, R. M. J., "Imperfection-Insensitive Continuous Tow-Sheared Cylinders," *Composites Structures*, Vol. 260, 2021, p. 113445. https://doi.org/10.1016/j.compstruct.2020.113445.

[36] Lincoln, R. L., Weaver, P. M., Pirrera, A., and Groh, R. M. J., "Optimization of Imperfection-Insensitive Continuous Tow Sheared Rocket Launch Structures," *AIAA SciTech 2021 Forum and Exposition*, 2021. https://doi.org/10.2514/6.2021-0202, Paper Nr. 2021-0202.

[37] Lincoln, R. L., Weaver, P. M., Pirrera, A., and Groh, R. M. J., "Manufacture and Buckling Test of a Variable-Stiffness, Variable-Thickness Composite Cylinder under Axial Compression," *AIAA SciTech 2022 Forum and Exposition*, 2022. https://doi.org/10.2514/6.2022-0664, Paper Nr. 2022-0664.

[38] Labans, E., Abramovich, H., and Bisagni, C., "An Experimental Vibration-Buckling Investigation on Classical and Variable Angle Tow Composite Shells Under Axial Compression," *Journal of Sound and Vibration*, Vol. 449, 2019, pp. 315–329. https://doi.org/10.1016/j.jsv.2019.02.034.

[39] Coburn, B. H., Wu, Z., and Weaver, P. M., "Buckling Analysis of Stiffened Variable Angle Tow Panels," *Composite Structures*, Vol. 111, 2014, pp. 259–270. https://doi.org/10.1016/j.compstruct.2013.12.029.

[40] Stodieck, O., Cooper, J. E., Weaver, P. M., and Kealy, P., "Improved Aeroelastic Tailoring Using Tow-Steered Composites," *Composite Structures*, Vol. 106, 2013, pp. 703–715. https://doi.org/10.1016/j.compstruct.2013.07.023.

[41] Stodieck, O., Cooper, J. E., Weaver, P. M., and Kealy, P., "Optimization of Tow-Steered Composite Wing Laminates for Aeroelastic Tailoring," *AIAA Journal*, Vol. 53, No. 8, 2015, pp. 2203–2215. https://doi.org/10.2514/1.J053599.

[42] Stodieck, O., Cooper, J. E., Weaver, P. M., and Kealy, P., "Aeroelastic Tailoring of a Representative Wing Box Using Tow-Steered Composites," *AIAA Journal*, Vol. 55, No. 4, 2017, pp. 1425–1439. https://doi.org/10.2514/1.J055364.

[43] Stanford, B. K., and Jutte, C. V., "Comparison of Curvilinear Stiffeners and Tow Steered Composites for Aeroelastic Tailoring of Aircraft Wings," *Computers & Structures*, Vol. 183, 2017, pp. 48–60. https://doi.org/10.1016/j.compstruc.2017.01.010.

[44] Oliveri, V., Zucco, G., Peeters, D., Clancy, G., Telford, R., Rouhi, M., McHale, C., O'Higgins, R. M., Young, T. M., and Weaver, P. M., "Design, Manufacture and Test of an In-Situ Consolidated Thermoplastic Variable-Stiffness Wingbox," *AIAA Journal*, Vol. 57, No. 4, 2019, pp. 1671–1683. https://doi.org/10.2514/1.J057758.

[45] Liguori, F. S., Zucco, G., Madeo, A., Magisano, D., Leonetti, L., Garcea, G., and Weaver, P. M., "Postbuckling Optimisation of a Variable Angle Tow Composite Wingbox Using a Multi-Modal Koiter Approach," *Thin-Walled Structures*, Vol. 138, 2019, pp. 183–198. https://doi.org/10.1016/j.tws.2019.01.035.

[46] Wang, Z., Wan, Z., Groh, R. M. J., and Wang, X., "Aeroelastic and Local Buckling Optimisation of a Variable-Angle-Tow Composite Wing-Box Structure," *Composites Structures*, Vol. 258, 2021, p. 113201. https://doi.org/10.1016/j.compstruct.2020.113201.

[47] Çelebi, M., Gürdal, Z., Tatting, B., Blom-Schieber, A., Rassaian, M., Wanthal, S., and Türkmen, H. S., "Bending of Composite Cylindrical Shells with Circular Cutouts: Buckling and Failure Analysis," *Journal of Aircraft*, Vol. 56, No. 4, 2019. https://doi.org/10.2514/1.C035246.

[48] Labans, E., Bisagni, C., Çelebi, M., Tatting, B., Gürdal, Z., Blom-Schieber, A., Rassaian, M., and Wanthal, S., "Bending of Composite Cylindrical Shells with Circular Cutouts: Experimental Validation," *Journal of Aircraft*, Vol. 56, No. 4, 2019. https://doi.org/10.2514/1.C035247.

[49] Wu, K. C., "Design and Analysis of Tow-Steered Composite Shells Using Fiber Placement," *Proceedings of the ASC 23rd Annual Technical Conference*, Memphis, TN, USA, 2008. https://doi.org/10.2514/6.2009-2700, Paper Nr. 125.

[50] Wu, K. C., Tatting, B. F., Smith, B. H., Stevens, R. S., Occhipinti, G. P., Swift, J. B., Achary, D. C., and Thornburgh, R. P., "Design and Manufacturing of Tow-Steered Composite Shells Using Fiber Placement," *Proceedings of the 50th AIAA/ASME/ASCE/AHS/ASC Structures, Structural Dynamics and Materials Conference*, Palm Springs, CA, USA, 2009. https://doi.org/10.2514/6.2009-2700, Paper Nr. 2009-2700.

[51] Wu, K. C., Farrokh, B., Stanford, B. K., and Weaver, P. M., "Imperfection Insensitivity Analyses of Advanced Composite Tow-Steered Shells," *AIAA SciTech 2016 Forum and Exposition*, San Diego, CA, USA, 2016. https://doi.org/10.2514/6.2016-1498, Paper Nr. 2016-1498.

[52] Wu, K. C., Turpin, J. D., Stanford, B. K., and Martin, R. A., "Structural Performance of Advanced Composite Tow-Steered Shells with Cutouts," *AIAA SciTech 2014 Forum and Exposition*, National Harbor, MD, USA, 2014. https://doi.org/10.2514/6.2014-1056, Paper Nr. 2014-1056.

[53] Wu, K. C., Turpin, J. D., Gardner, N. W., Stanford, B. K., and Martin, R. A., "Structural Characterization of Advanced Composite Tow-Steered Shells with Large Cutouts," *AIAA SciTech 2015 Forum and Exposition*, Kissimmee, FL, USA, 2015. https://doi.org/10.2514/6.2015-0966, Paper Nr. 2015-0966.

[54] *ABAQUS 2018 Standard User's Manual*, Dassault Systèmes Simulia Corp, United States, 2018.

[55] Hilber, H. M., Hughes, T. J. R., and Taylor, R. L., "Improved Numerical Dissipation for Time Integration Algorithms in Structural Dynamics," *Earthquake Engineering and Structural Dynamics*, Vol. 5, 1977, p. 283–292. https://doi.org/10.1002/eqe.4290050306.

[56] Hilburger, M. W., and Starnes Jr., J. H., "Effects of Imperfections on the Buckling Response of Compression-Loaded Composite Shells," *International Journal of Nonlinear Mechanics*, Vol. 37, 2002, pp. 623–643. https://doi.org/10.1016/S0020-7462(01)00088-9.

[57] Wohlever, J. C., and Healey, T. J., "A Group Theoretic Approach to the Global Bifurcation Analysis of an Axially Compressed Cylindrical Shell," *Computer Methods in Applied Mechanics and Engineering*, Vol. 122, 1995, pp. 315–349. https://doi.org/10.1016/0045-7825(94)00734-5.

[58] Groh, R. M. J., and Pirrera, A., "On the Role of Localizations in Buckling of Axially Compressed Cylinders," *Proceedings of the Royal Society A*, Vol. 475, 2019, p. 20190006. https://doi.org/10.1098/rspa.2019.0006.

[59] Groh, R. M. J., Hunt, G. W., and Pirrera, A., "Snaking and Laddering in Axially Compressed Cylinders," *International Journal of Mechanical Sciences*, Vol. 196, 2021, p. 106297. https://doi.org/10.1016/j.ijmecsci.2021.106297.

[60] Groh, R. M. J., and Pirrera, A., "Spatial Chaos as a Governing Factor for Imperfection Sensitivity in Shell Buckling," *Physical Review E*, Vol. 100, 2019, p. 032205. https://doi.org/10.1103/PhysRevE.100.032205.